energies

MDPI

Article

Ab Initio Modeling of $CuGa_{1-x}In_xS_2$, $CuGaS_{2(1-x)}Se_{2x}$ and $Ag_{1-x}Cu_xGaS_2$ Chalcopyrite Solid Solutions for Photovoltaic Applications

Jurij Grechenkov [1], Aleksejs Gopejenko [1], Dmitry Bocharov [1,2], Inta Isakoviča [1], Anatoli I. Popov [1,3], Mikhail G. Brik [1,4,5,6,7,8] and Sergei Piskunov [1,*]

1 Institute of Solid State Physics, University of Latvia, 8 Kengaraga Str., LV-1063 Riga, Latvia; grecenkovs@cfi.lu.lv (J.G.); agopejen@cfi.lu.lv (A.G.); bocharov@cfi.lu.lv (D.B.); intai@cfi.lu.lv (I.I.); popov@cfi.lu.lv (A.I.P.); mikhail.brik@cfi.lu.lv or mikhail.brik@ut.ee (M.G.B.)
2 Transport and Telecommunication Institute, LV-1019 Riga, Latvia
3 Department of Technical Physics, L.N. Gumilyov Eurasian National University, Nur-Sultan 010008, Kazakhstan
4 Institute of Physics, University of Tartu, W. Ostwald Str. 1, 50411 Tartu, Estonia
5 College of Sciences & CQUPT-BUL Innovation Institute, Chongqing University of Posts and Telecommunications, Chongqing 400065, China
6 Faculty of Science and Technology, Jan Dlugosz University, Armii Krajowej 13/15, PL-42200 Czestochowa, Poland
7 Academy of Romanian Scientists, Ilfov Str. No. 3, 050044 Bucharest, Romania
8 Centre of Excellence for Photoconversion, Vinča Institute of Nuclear Sciences-National Institute of the Republic of Serbia, University of Belgrade, 11351 Belgrade, Serbia
* Correspondence: piskunov@cfi.lu.lv

Abstract: Chalcopyrites are ternary semiconductor compounds with successful applications in photovoltaics. Certain chalcopyrites are well researched, yet others remain understudied despite showing promise. In this study, we use ab initio methods to study $CuGaS_2$, $AgGaS_2$, and $CuGaSe_2$ chalcopyrites with a focus on their less studied solid solutions. We use density functional theory (DFT) to study the effects that atomic configurations have on the properties of a solid solution and we calculate the optical absorption spectra using a many-body perturbation theory. Our theoretical simulations predict that excess of In and Se in the solid solutions leads to narrowing of the band gap and to the broadening of the absorption spectra. Obtained results show promise for possible photovoltaic applications, as well as developed methodology can be used for further study of other promising chalcopyritic compounds.

Keywords: chalcopyrites; solid solutions; density functional theory; ab initio calculation; photovoltaics

Citation: Grechenkov, J.; Gopejenko, A.; Bocharov, D.; Isakoviča, I.; Popov, A.I.; Brik, M.G.; Piskunov, S. Ab Initio Modeling of $CuGa_{1-x}In_xS_2$, $CuGaS_{2(1-x)}Se_{2x}$ and $Ag_{1-x}Cu_xGaS_2$ Chalcopyrite Solid Solutions for Photovoltaic Applications. *Energies* **2023**, *16*, 4823. https://doi.org/10.3390/en16124823

Academic Editor: Philippe Leclère

Received: 25 April 2023
Revised: 13 June 2023
Accepted: 14 June 2023
Published: 20 June 2023

1. Introduction

Chalcopyrites are ternary semiconductor materials with a general formula I–III–VI_2 or II–IV–V_2. They are well known for their thin film solar cell applications with copper indium gallium diselenide (CIGS) being an efficiency record holder for multiple decades [1–3], although recently there is competition from perovskite and cadmium telluride technologies [4]. An important caveat about CIGS is that it is not a pure chalcopyrite but a solid solution of $CuInSe_2$ and $CuGaSe_2$. Precise control over In/Ga composition allows for band gap tuning and is thus paramount in achieving the desired solar cell efficiency.

Chalcopytite solar cells are typically manufactured by the deposition of metals on a substrate either by evaporation or sputtering with a subsequent sulfurization or selenization step [5]. Another approach is the use of epitaxial methods, where growth and composition are dictated by the temperature inside the effusion cells, thus giving the control of the final product [6]. Under these circumstances, the composition of a final solid solution is set either by mixture proportion of the precursor chemicals in the case of the evaporative method or by

controlling the fluxes in epitaxy. The band gap of an obtained solid solution and most of its properties, in general, vary gradually between those of the endpoint compounds, provided that the constituent has similar chemical nature and are interchangeable in the crystal lattice. Precisely, this fact allows for band gap engineering with one of the first historical examples in semiconductor technology being the experiments with silicon-germanium alloys [7]. For CIGS, the typical Gallium to Indium proportion is approximately 0.4, which leads to improved device performance, although the optimal band gap is at a higher gallium concentration [8].

Analogously, other chalcopyrite-like (kesterite [9]) compounds were proposed as candidates for photovoltaic applications; copper zinc tin sulfide (CZTS), copper zinc tin selenide (CZTSe), and their respective solid solutions (CZTSSe) are actively studied in an attempt to replace toxic and/or expensive materials, such as indium, gallium, and tellurium [10,11]. The photovoltaic effect was first demonstrated in 1988 [12], but recently the interest has grown due to improving the efficiency of the solar cells fabricated by this technology [4]. Just as in the case of CIGS, zinc to tin proportion may be controlled to reach a desired band gap value, and, thus, desirable optical absorption properties can be obtained. Practically used chemical composition is close to stoichiometric ($Cu_2ZnSnSe_4$), and the record efficiency for this type of solar cell are on the order of 12% [4,13].

Chalcopyrite-like compounds with copper replaced by silver and gold are also a research topic. Gold-containing chalcopyrites have been investigated theoretically [14] and the presence of copper-gold domains was shown to have a beneficial impact on transport properties in $CuInS_2$ solar cells [15]. Silver-containing chalcopyrites on the other hand have interesting non-linear optical properties and are developed as an ecologically friendly alternative to existing solar cells.

Chalcopyrite applications are not limited to photovoltaics. Lithium-containing compounds demonstrate birefringence and together with aforementioned $AgGaSe_2$ show non-linear optical properties [16–19]. Enriched $LiInSe_2$ is being explored for neutron scintillating applications due to the high neutron cross-section of ^6Li and natively exhibited luminescence [20,21]. Although it is worth mentioning that this material under normal conditions crystallizes in a structure that is atypical for chalcopyrites.

In summary, chalcopyrites present some compelling properties and deserve further investigation. Considering theoretical computational methods may be more practical than the direct experimental research, which can prove expensive and technically challenging. In the presented work we employ the density functional theory (DFT) methods to study the atomic, electronic, and optical properties of chalcopyrite solid-state solutions.

Previous studies are either based on pure chalcopyritic compounds [22–28] or treat solid solutions for a select few possible elemental compositions [29]. Anyway, a comprehensive analysis of chalcopyritic solid solutions to our knowledge was not yet performed and certain data points are lacking. We aim, therefore, with our work to plug the gaps in the existing knowledge.

The broad class of ternary metal/non-metal semiconductors crystallize in tetragonal, orthorhombic, trigonal, or cubic symmetry [30], yet compounds that are classified as chalcopyrites and are important for photovoltaic applications are tetragonal, have the $I\bar{4}2d$ space group (Nr. 122), and, henceforth, will be the only ones considered.

The paper is organized in the following way. First, we discuss the utilized methods and underlying reasons for the choice of each of the used DFT-based approaches, next, the results are presented, starting with calculations for different possible configurations for solid solution crystallographic cell, and then the calculated electronic and optical properties of the materials. The paper ends with a brief discussion of the results.

2. Computational Details

Striving for generality we considered the solid solutions with a general formula of $Cu_xAg_{1-x}Ga_yIn_{1-y}S_{2z}Se_{2(1-z)}$ that is solid solutions that are formed when one of the

elements in $CuGaS_2$ is partially replaced. In this case x, y, and z run from 0 to 1 and define a three-dimensional configuration space.

A single pure chalcopyrite crystallographic cell contains four times as many atoms as defined by stoichiometry in the chemical formula. Hence, by exchanging atoms inside the crystallographic cell one can achieve different compositions for solid solutions with a step of 0.25 (or 0.125 for group VI atoms) for the above-defined configuration coordinates. It is important to note that there is a number of non-equivalent positions an atom may take in the crystallographic cell. One of the focuses of our study was to understand the effect of the non-equivalent positioning of atoms on the overall electronic properties of the material.

Secondly, one of the determining factors for photovoltaic applications is the absorption efficiency. Interpreted as the imaginary part of the dielectric function, the absorption efficiency can be obtained using perturbation theory applied to previously calculated electronic wave functions. This is technically done using Green function formalism and solving the Dyson equation for the microscopic dielectric susceptibility. The microscopic dielectric susceptibility is then defined by an expression [31,32]:

$$\chi_{G,G'}(q,\omega) = \chi^0_{G,G'}(q,\omega) + \sum_{G_1,G_2} \chi^0_{G,G_1}(q,\omega) v_{G_1} \delta_{G_1,G_2} \chi_{G_2,G}(q,\omega)$$

where $\chi_{G,G'}$—is the final susceptibility in random phase approximations, $\chi^0_{G,G'}$ is the unperturbed susceptibility, v—the Hartree potential and q and ω are the transferred momenta and frequency. The microscopic dielectric function is connected to the microscopic susceptibility through a formula:

$$\epsilon^{-1}_{G,G'} = \delta_{G,G'} + v_G(q)\chi_{G,G'}(q,\omega)$$

The macroscopic dielectric function is then found by taking the limit as $q \to 0$. This approximation omits additional effects, such as two particle interaction, which can lead to exciton formation that moves the optical absorption edge deeper into the band gap region and can play a role in the description of the absorption spectra of the material. Furthermore, only the Hartree part of the exchange-correlation is taken into account, which can lead to the reduced accuracy of the results.

For the calculation of electronic band structures and estimation of the role of atomic position in the crystallographic cell, we utilized total energy code CRYSTAL [33,34] owing to its computational efficiency and the exploitation of linear combination of atomic orbitals (LCAO)-based methods for basis sets that are known to produce good results for non-conducting materials [35]. However, since the optical properties calculations are poorly represented in CRYSTAL code, we employ Quantum Espresso and Yambo bundle [31,36,37] to obtain the dielectric functions.

2.1. Electronic Band Structure

Consistent triple zeta value basis sets with polarization quality [38] were considered for application in the study. These basis sets were tested against a variety of materials, including different metal chalcogens, which are relevant to our study. In the test calculations, they provided fast and robust self-consistent field computation convergence and reliable lattice constant values with a maximum deviation from the experiment of no more than 3% for the complete material test set. Therefore, in a natural attempt to capture the precise results and to optimize convergence times we used the aforementioned basis sets for all our computations.

In order to choose the best suited exchange-correlation functional we performed a series of test runs that are summarized in Tables 1 and 2. $CuGaS_2$ and $CuGaSe_2$ were used as test cases and both the deviation of lattice constants and the band gap values from experimental observations was used to gauge the quality of the representation provided by the chosen functionals. Of all the juxtaposed functionals HSE06 [39] was chosen as the most fitting from the results of calculations.

HSE06 is a hybrid functional that mix the GGA functional with a portion of exact Hartree–Fock exchange. HSE06 specifically incorporates a screened Coulomb interaction to improve the description of the exchange term and it is well-suited for computations of semiconductor materials.

Our test runs demonstrated the best agreement for both lattice constant and band gap values. Lattice constants are within 4‰ of the experimental value, yet the band gap value differs as much as 1 eV, which is, however, a well-known imprecision of the DFT method.

For every compound, we started with a geometry input where lattice constants were set using available experimental data. Geometry was subsequently optimized using the BFGS algorithm [40]. For solid solutions the crystallographic cell used for calculation was expanded to a desired volume and the necessary admixture was created by utilizing the atomic substitution functionality provided by CRYSTAL. The best performance was achieved by using the Anderson method for convergence acceleration and an FMIXING (a parameter that defines Fock/Kohn–Sham matrix mixing) value of 80%.

Table 1. Lattice constants and band gap for $CuGaS_2$ compound obtained with functionals B3PW [41–43], B3LYP [44–46], HSE06 [39,47], PBE0 [48], and SC-BLYP [49].

$CuGaS_2$	a, (Å)	c, (Å)	Band Gap, (eV)
B3PW	5.37	10.53	3.23
B3LYP	5.45	10.64	2.95
HSE06	5.36	10.51	3.10
PBE0	5.36	10.50	3.77
SC-BLYP	5.49	10.71	2.35
Experiment [3]	5.35	10.47	2.53

Table 2. Lattice constants and band gap for $CuGaSe_2$ compound obtained with with functionals B3PW [41–43], B3LYP [44–46], HSE06 [39,47], PBE0 [48], and SC-BLYP [49].

$CuGaSe_2$	a, (Å)	c, (Å)	Band Gap, (eV)
B3PW	5.63	11.08	2.86
B3LYP	5.70	11.23	2.54
HSE06	5.62	11.05	2.66
PBE0	5.61	11.04	3.30
SC-BLYP	5.74	11.31	1.98
Experiment [50]	5.61	11.02	1.63

2.2. Optical Properties

To obtain the absorption spectra we utilized Yambo code [31,37] which, however, is not interfaced with CRYSTAL output and so additional self-consistent calculations had to be performed to obtain usable wavefunctions.

For the correct implementation of the Yambo code, it is necessary to obtain the wavefunctions that are constructed from a norm-conserving basis set. In order to assure this we used pw.x (PWSCF) utility from the Quantum Espresso code [36] and the norm-conserving pseudopotential plane wave basis set with an energy cut-off of 30 Rydberg [51]. In this work, authors generated a set of 141 norm-conserving pseudo potentials split into the stringent and standard accuracy tables for the most abundant periodic table elements. The authors gave special care to test the validity of the provided potentials with the total number of test calculations being 70,000. In our study, we used the standard accuracy pseudopotentials, which in our tests lead to faster convergence of the results.

A pure DFT correlation-exchange functional, namely, the Perdew–Burke–Ernzerhof (PBE) functional, was used [52] as the basis for pw.x calculations due to the faster convergence times.

Calculations were performed using $6 \times 6 \times 6$ k-point mesh. To achieve faster convergence, we utilized Davidson iterative diagonalization with an overlap matrix mixing beta

of 0.6. The space group was forced to be symmorphyc (only symmmorphic symmetries were used in calculation), which was necessary for the correct functioning of the further optical spectra calculation module. Geometry optimization was performed on the system using the BFGS (Broyden–Fletcher–Goldfarb–Shanno) algorithm, with the convergence of the optimization step proving more challenging than in the case of CRYSTAL computations.

Compared with experimental results we obtained underestimated band values with the observed error in the range of 1 eV, and, in general, the band gap values were less accurate than the one obtained in CRYSTAL calculations with an optimized hybrid functional choice. The lattice constants, however, agreed well with available experimental data and were within few percent of the reported values.

Typical calculation lasted much longer than the analogous counterpart in CRYSTAL, and the overall computational time increased by a factor of ten. The especially long conversion was observed for the cases with selenium present in the computation. We attribute this fact to the choice of pseudopotential.

We used Yambo, a tool based on perturbation theory, that obtains the dielectric function by solving the Dyson equation for electric susceptibility. For the calculation of the electric susceptibility functions, we used the independent particle approximation with application of scissor operator to correct for band gap discrepancies compared to calculations made with CRYSTAL. Since the crystal has an anisotropic tetragonal crystal structure we provide spectra calculated for the two principle directions in the crystal, the electric field is either applied parallel to the longer crystal axis (*c*) or orthogonal to it (along the direction *a*). The damping factor was set to 0.1 eV, and the spectra were calculated in the 0 to 10 eV frequency range for 1000 energy steps between the boundary points. This range captures the totality of the visible spectrum range and depicts all the essential interesting absorption characteristics of these materials.

3. Results and Discussion

3.1. Atomic Structure

As mentioned before, when considering a solid solution there are multiple atom placement possibilities in a crystallographic cell. We studied the effect that the different positioning of Ga and In atoms in a $CuGa_xIn_{1-x}S_2$ crystallographic cell can have on the calculation results. Under the chosen representation of the crystallographic cell for pure chalcopyrite ($CuGaS_2$ or $CuInS_2$, see Table 3) all Cu atoms are located in the Wyckoff *a* position, Ga and In are in Wyckoff position *b*, while S remains in the position *d*. In other words since the positions of Ga and In are symmetrically equivalent, the substitution of a single atom inside the crystallographic cell is invariant for any of the four available placement positions. This corresponds to the cases $CuGa_{0.25}In_{0.75}S_2$ and $CuGa_{0.75}In_{0.25}S_2$, where one of the atoms of the corresponding pure chalcopyrites is swapped with another one.

Table 3. Wyckoff positions for space group $I\bar{4}2d$ (Nr. 122).

Multiplicity	Wyckoff Letter	Site Symmetry	Coordinates (0, 0, 0) + (1/2, 1/2, 1/2)+
16	e	1	(x, y, z) (−x, −y, z) (y, −x, −z) (−y, x, −z) (−x+1/2, y, −z+3/4) (x + 1/2, −y, −z+3/4) (−y+1/2, −x, z+3/4) (y+1/2, x, z+3/4)
8	d	.2.	(x,1/4,1/8) (−x, 3/4, 1/8) (1/4, −x, 7/8) (3/4, x, 7/8)
8	c	2..	(0, 0, z) (0, 0, −z) (1/2, 0, −z+3/4) (1/2, 0, z+3/4)
4	b	−4..	(0, 0, 1/2) (1/2, 0, 1/4)
4	a	−4..	(0, 0, 0) (1/2, 0, 3/4)

On the other hand, when two atoms ought to be replaced, the underlying symmetry is broken, and the positioning of the atoms becomes non-equivalent. Therefore, we per-

formed calculations pertaining to all possible non-equivalent two atoms positioning inside a crystallographic cell to assess the effect that different configurations may have on the overall properties of the system.

Obtained results (Figure 1) show that possible configurations may be grouped in two general cases, one that preserves the tetragonal symmetry and one that breaks it. If the atoms are placed asymmetrically, the lattice becomes elongated in the direction corresponding to the greater concentration of larger diameter atoms, which leads to irregularities in the physical crystal. The band gap is also affected and is different in the two cases. Yet the overall effect is small corresponding to ≈1.5% for the case of band gap value differences and to ≈0.5% regarding the lattice anisotropy. Hence, in the first approximation different atom positioning is insignificant and can be disregarded.

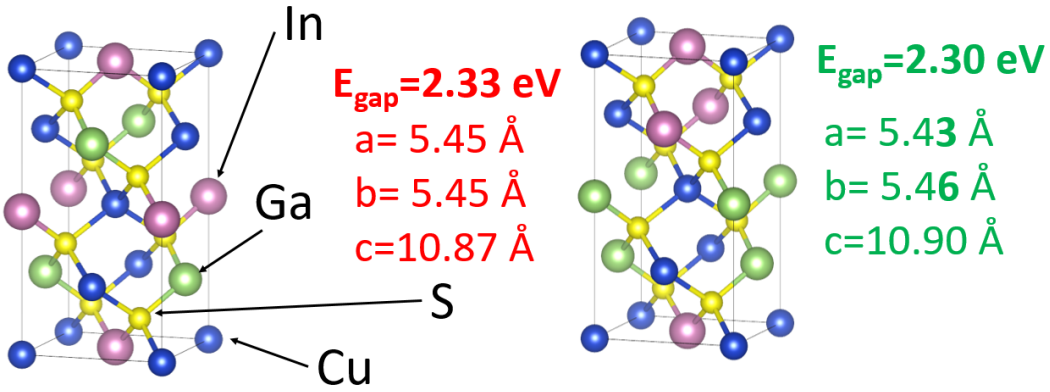

Figure 1. Possible atom positioning in a $CuGa_{0.5}In_{0.5}S_2$ cell. In red: symmetric lattices; in green: lattices with the broken tetragonal symmetry due asymmetric atomic placements.

Moreover, a real crystal should be considered as a mixture of these configurations, with the results smoothed over by the averaging effect of all configurations simultaneously present in the physical crystal. Since the range, in which the band gap values fluctuate, is constricted it is not depicted in Figure 2, instead the average value is used. The lattice constants as well are given for the symmetric case that does not break the tetragonal symmetry and are averaged over the obtained values for every of the calculated compositions.

3.2. Electronic and Optical Properties

Using the symmetrical atom configuration we have performed calculations for solid solutions with different chemical compositions. Results are gathered in Figure 2. Most of the parameters change linearly between the pure chalcopyrite states, yet there is a visible non-linearity for the case of band gap for Cu-Ag solid solution. We calculated the bowing parameter for the silver–copper solid solution and found it to be equal to approximately 80 meV. This may connected to the non-uniform change in the lattice parameters; while *a* increases *c* remains virtually unchanged, hence leading to a changing a/c ratio (from 1.94 to 1.84) and to a more pronounced tetragonal character of the $AgGaS_2$ crystal lattice. The a/c ratios for Indium–Gallium solid solution, on the other hand, changes from 1.94 to 1.98 linearly, and similarly, the a/c ratio for sulphur–selenium solution ranges between 1.94 and 1.96.

We also calculated the electronic band structures of the solid solutions under study. A selection of these results for pure materials and their mutual solutions are presented in Figure 3. The calculations were performed using the utilities provided by crystal code, and the path was chosen along the high-symmetry points for the $I\bar{4}2d$ group (Γ, *M*, *P*, *PA*) as defined by the Bilbao crystallography server [53].

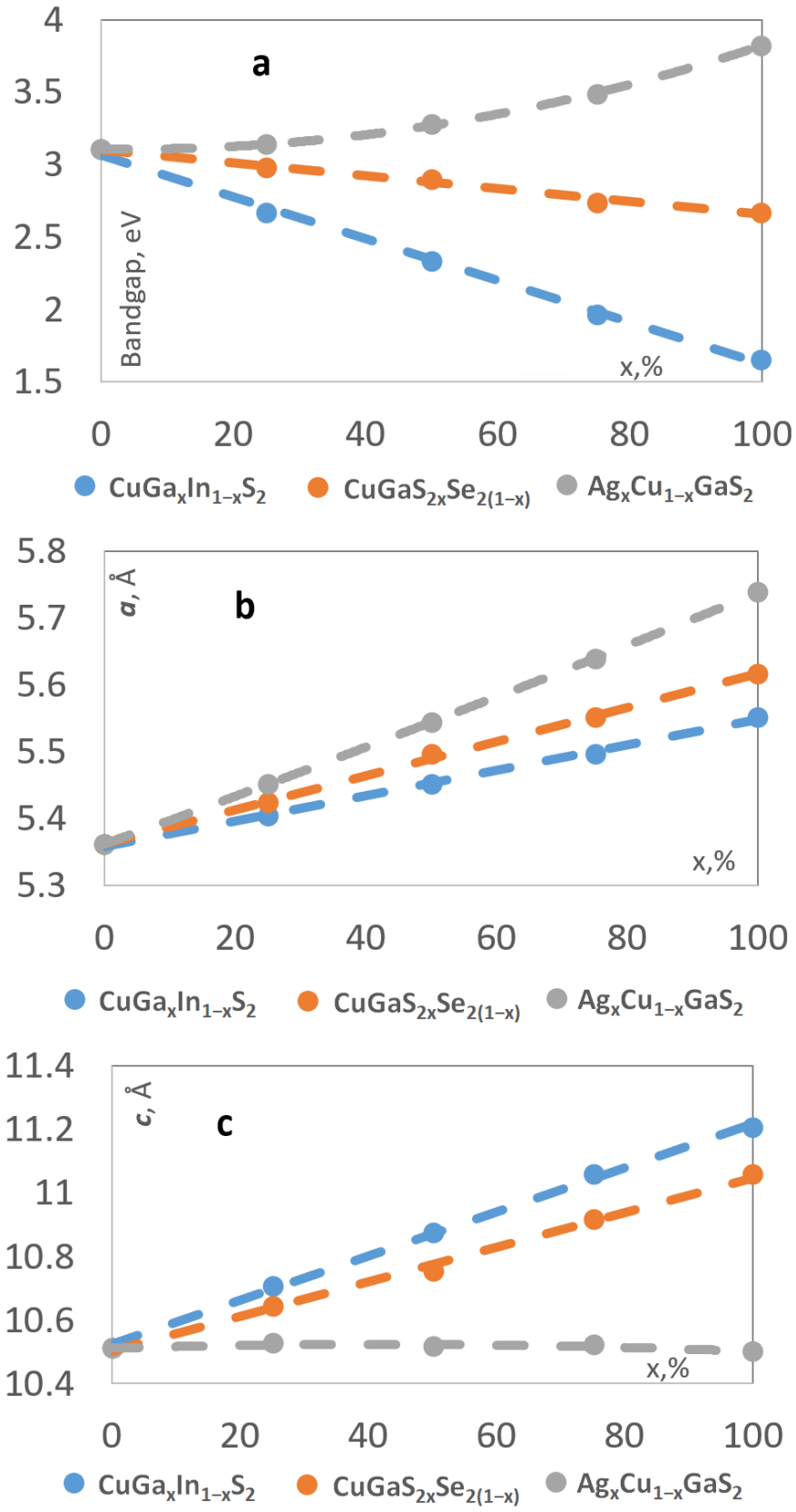

Figure 2. Band gaps (**a**) and lattice parameters (**b**,**c**) for $CuGa_{1-x}In_xS_2$, $CuGaS_{2(1-x)}Se_{2x}$ and $Ag_{1-x}Cu_xGaS_2$ solid solutions with different concentrations of Ga and In (blue curve), S and Se (orange curve) and An and Cu (gray curve) concentration. Linear approximation is used for all solutions except $Cu_xAg_{(1-x)}GaS_2$, where quadratic fit is used to account for the band gap bowing.

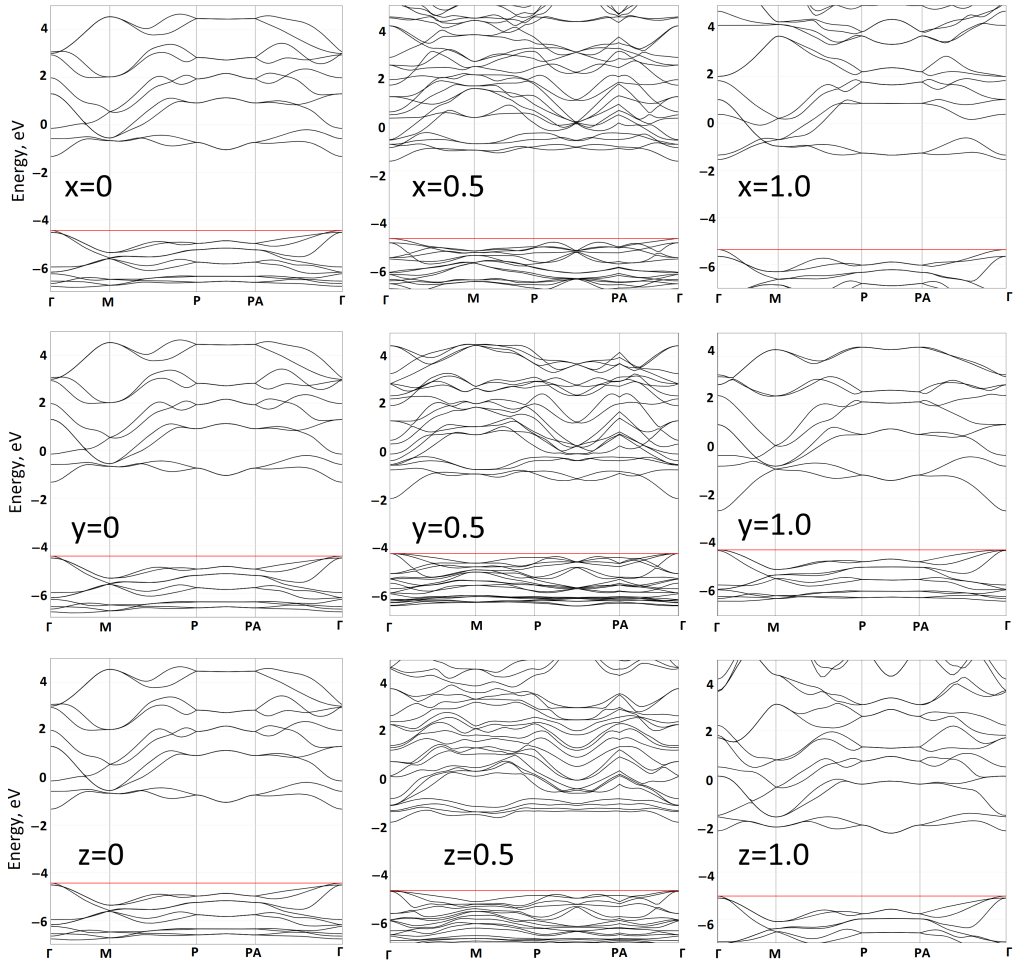

Figure 3. Calculated band structures. (**Top row**): $Cu_xAg_{1-x}GaS_2$, (**middle row**): $CuGa_yIn_{1-y}S_2$, (**bottom row**): $CuGaS_{2z}Se_{2(1-z)}$. The Fermi level is shown as calculated in comparison to vacuum energy. Energy scales and Brioulline zone paths are identical for all of the depicted compounds.

A direct Γ–Γ band gap is visible in the calculated band structures. It leads to the large absorption coefficient and again confirms the applicability of the materials for solar cell applications. Presence of In and Se in the solid solutions leads to the narrowing of the band gap shifting the band edges toward lower energies while presence of Ag increases the band gap.

Interpretation of the band structure near the band gap is as follows. For the case of a pure $CuGaInS_2$, the conduction band is formed by Gallium s-orbitals and sulphur s-orbitals, the valence band, on the other hand, is formed by the d-orbitals of copper and by the p-orbitals of sulphur. The addition of other constituents into the solid solutions introduces new orbitals into the band structure and newly formed bands are created as orbitals of the solution-forming elements hybridize with each other. Silver d-orbitals mix with copper d-orbitals (Figure 4), Gallium s-orbitals participate in the conduction band formation together with Indium-p orbitals, and selenium and sulphur p-orbitals influence both the valence and the conduction bands. Since, in general, for our study the band gap for the admixture chalcopyrites grows together with the atomic number of the constituent elements, the total effect on the band structure is the band gap reduction.

The Fermi level remains relatively unchanged between the various solid solutions with a notable exception of silver, which leads to a noticeable decrease in the Fermi level. Near the Γ-point the valence and conduction bands are flat, which is to be expected for a photovoltaic material. The curvature of the conduction and valence bands does not also

significantly change with the introduction of other elements, which is desirable for solar cell applications, such as reduced charge carrier effective mass and higher mobility.

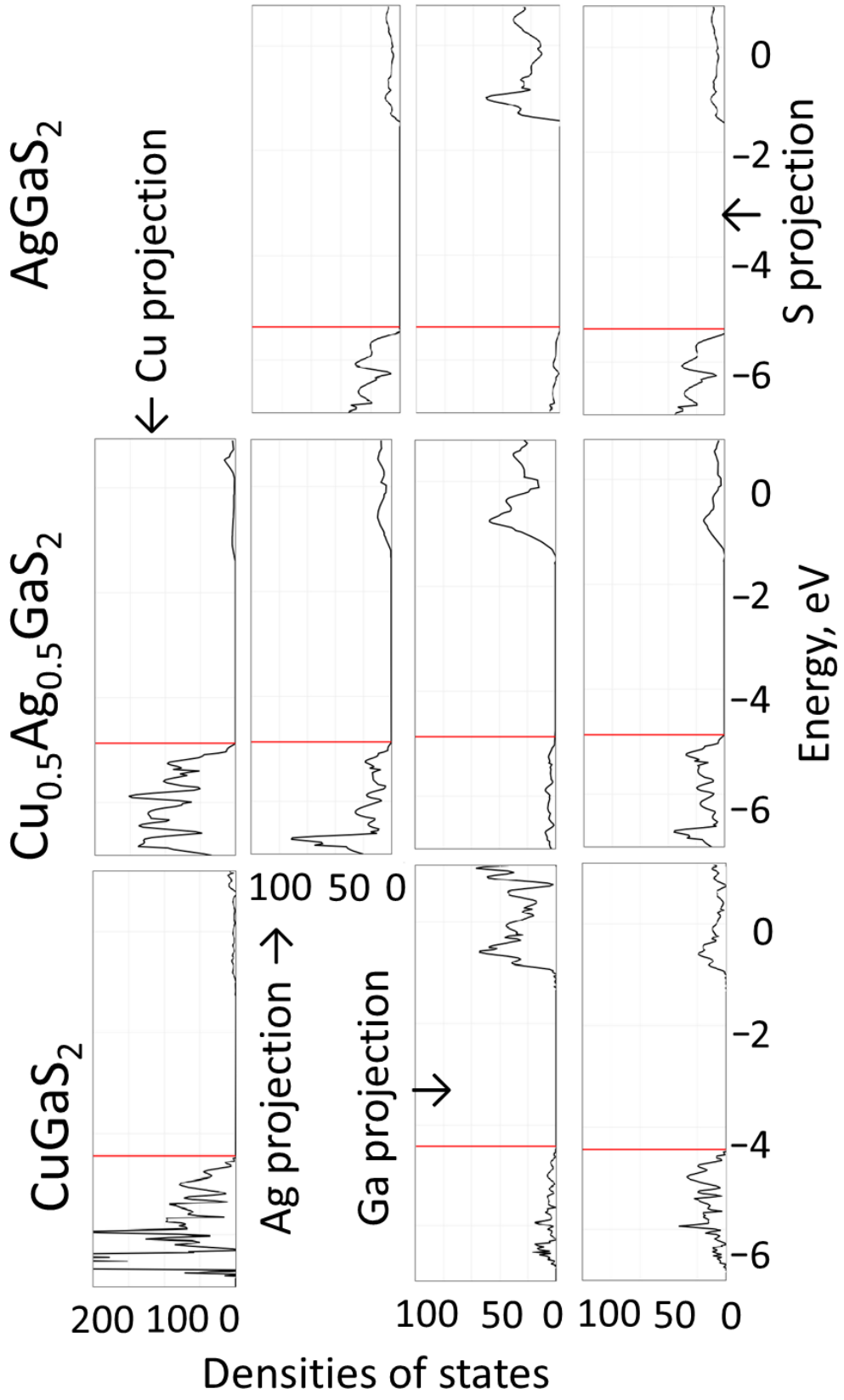

Figure 4. Projected density of states for the case of copper–silver solid solution. Columns represent increasing silver admixture, rows—projections of densities of states on different elemental species.

Lastly, we have performed calculations of optical absorption spectra. Figure 5 shows spectra obtained using Yambo code for different compositions of solid solutions. The absorption as expected starts in the visible light region and diminishes past its peak until the 10 eV mark is reached. This range defines most of the total absorption range for the materials. The broadening of absorption spectra for $CuGa_{1-x}In_xS_2$, $CuGaS_{2(1-x)}Se_{2x}$ solid solutions is predicted. The results are in reasonable agreement with experimental and other theoretical predictions and experimental data [54–57]. Compared to the available data we correctly represent the absorption edge in our calculations. For $CuInS_2$, we find a peak near 2 eV that can correspond to the increase in absorbance found in spectra from the literature, that does not, however, appear as sharply in the experiment and is smeared. The characteristic valley near the 8 eV is also attested for in experimental data.

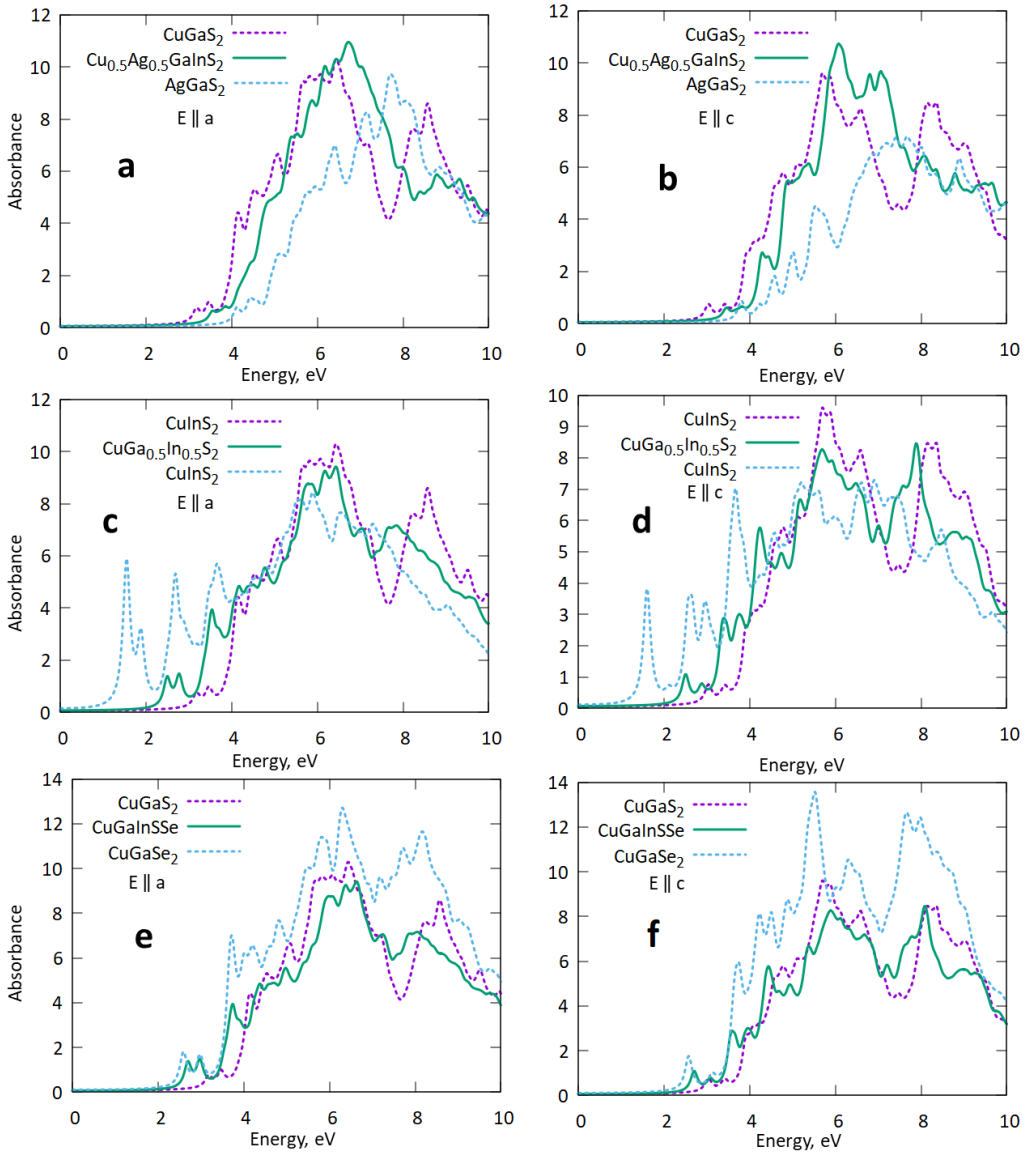

Figure 5. Imaginary part of the dielectric function for the solid solutions. (**a**,**b**)—silver–copper solid solution, (**c**,**d**)—Ga–In solid solution, (**e**,**f**)—S–Se solid solution. Solid lines represent the 50% solid solutions and the dashed lines are the corresponding pure materials. The left column depicts results for the electric field oriented along the *a* crystal axis ($E \parallel a$) and the right column—the electric field along the *c* crystallographic axis ($E \parallel c$).

4. Discussion

The agreement with the experimental data raises confidence in the correct application of the DFT methods for the calculation of the electronic and optical properties of the solid solution of chalcopyrites. By fine-tuning the methodology we aim to use this knowledge in future large scale high throughput calculations of chalcopyrite materials in hope of finding suitable candidates for future solar cell research.

The considered solid solution space is comprehensive in that it covers all three possible ion replacements for the copper gallium disulphide. It is, therefore, reasonable to expect that some of the points inside this space can be reached by linear interpolation between the already considered compounds. In this way, additional properties may be predicted. This improves further the predictive power of our results.

We used different computational codes with different approaches to the DFT calculations, namely, the LCAO and hybrid functional-based approach of CRYSTAL and the plane-wave based pure DFT approach as represented by Quantum Espresso calculations. This duality of methods allowed us to make a comparison between the two. At least in our case, the calculations performed by CRYSTAL were by an order of magnitude more computationally effective. The careful choice of hybrid functional also opened a possibility to a more accurate band gap prediction, and improves the agreement between the calculated and experimentally observed lattice constants.

On the other hand, the open-source nature of Quantum Espresso provides an access to more comprehensive optical property simulations through interfacing with other computational tools, viz. the capabilities offered by Yambo, yet therein also lies one of the possible weaknesses of our research; although we find our results to be sufficiently precise, an improvement may be achieved by utilizing more advanced use cases of the many-body perturbative theory methods. Excitonic effects might be taken into account using the Bethe–Saltpeter equation formalism [58], and the band gap prediction can be made more accurate using the GW approximation [59]. Further work will concentrate on developing these particular aspects, as well as in the broadening of the class of the considered materials, for which these effects may prove more significant.

The results of the calculations for the non-equivalent positions of atoms inside the crystallographic cell provide confidence in the applicability of the method to the prediction of electronic and optical properties of the chalcopirytic solid solutions. The discrepancies between the calculated configurations are small, and so the calculated results are, in general, only loosely dependent on a chosen configuration. The breaking of the tetragonal symmetry for some of the configurations points to possible interesting properties compared for a mixed material compared to a pure compound. For example, one can expect that the breaking of symmetry can lead to an observable difference in the phonon spectra.

A more comprehensive study can also include a greater variety of admixture concentrations. This would require a larger computational cell and could lead to additional effects for the newly obtained configurations for the case of a larger cell. For example, a cell with a twofold larger volume than the one considered in our study could provide results for a given metal concentration in the solid solution of 0.125. These changes, however, are expected to be inconsequential and have an even smaller impact on the overall properties of the material. Moreover, with a growing computational cell size some of the configurations become less thermodynamically and energetically favorable, and, thus, should have a smaller presence in the physical crystal, which further diminishes the significance of such calculations.

Overall, all of the considered compounds can be used for solar cell design with a correct constituent element ratio leading to a band gap value that is more suitable for photovoltaic applications. The implicit understanding is, however, that the knowledge of the electronic and optical properties of an ideal material is insufficient for a successful design of a highly efficient solar cell. Other factors to consider are the intrinsic and externally introduced defects, ease of manufacturing, mutual interaction with other materials inside the device, and economical and environmental considerations. Nevertheless, such theoretical studies

as this one should at least partly alleviate the difficulties in the search for the optimal photovoltaic material.

5. Conclusions

Using the theoretical approach described in this study the atomic, electronic, and optical properties of solid solutions of chalcopyrite materials can be successfully predicted from the first principles.

Calculations were performed using two different codes (Quantum Espresso and Yambo) and two different approaches (plane wave and linear combination of atomic orbitals), one used for band structure calculation, and the other for optical properties calculations. The text provides a comparison between the two.

In the calculations, the impact of atomic position inside a solid solution crystallographic cell leads to the possible breaking of tetragonal symmetry yet the effect is small, but, in general, can be neglected for the bulk phase calculations due insignificance of a configuration choice on the final result.

The dependence of band gap values and lattice constants is mostly linear for the considered compounds with a notable exception of Cu–Ag solid solution, for which the bowing parameter is 80 meV.

Considered compounds show properties suitable for solar cell applications. Chalcopyrites show great promise in the field of photovoltaics and, hopefully, the methodology developed here can be applied for a high throughput calculation of possible candidates for solar cell applications.

Author Contributions: Conceptualization, J.G., S.P., A.I.P., A.G., M.G.B. and D.B.; methodology, J.G., A.G., S.P. and D.B.; software, J.G.; validation, J.G., A.G., A.I.P., M.G.B., S.P. and D.B.; formal analysis, A.G. and J.G.; investigation, J.G.; resources, S.P.; data curation, J.G.; writing—original draft preparation, J.G. and D.B.; writing—review and editing, J.G., A.G., S.P., A.I.P., M.G.B., I.I. and D.B.; visualization, J.G.; supervision, S.P. and D.B.; project administration I.I.; funding acquisition: S.P. All authors have read and agreed to the published version of the manuscript.

Funding: This research is funded by the Latvian Council of Science grant No. LZP-2021/1-0322 (Large-scale computer modelling of defective ternary chalcopyrites for photovoltaic applications). All calculations were performed on Latvian Supercomputer Cluster (LASC) located at Institute of Solid State Physics in Riga. Institute of Solid State Physics, University of Latvia as the Center of Excellence has received funding from the European Union's Horizon 2020 Framework Programme H2020-WIDESPREAD-01-2016-2017-TeamingPhase2 under grant agreement No. 739508, project CAMART^2. M.G.B. also acknowledges the funding from Ministry of Science, Technological Development, and Innovation of the Republic of Serbia (451-03-47/2023-01/200017).

Data Availability Statement: Data will be made available on request.

Conflicts of Interest: The authors declare no conflict of interest.

References

1. Siebentritt, S. Chalcopyrite compound semiconductors for thin film solar cells. *Curr. Opin. Green Sustain. Chem.* **2017**, *4*, 1–7. [CrossRef]
2. Soni, A.; Gupta, V.; Arora, C.; Dashora, A.; Ahuja, B. Electronic structure and optical properties of $CuGaS_2$ and $CuInS_2$ solar cell materials. *Sol. Energy* **2010**, *84*, 1481–1489. [CrossRef]
3. Tell, B.; Shay, J.L.; Kasper, H.M. Electrical Properties, Optical Properties, and Band Structure of $CuGaS_2$ and $CuInS_2$. *Phys. Rev. B* **1971**, *4*, 2463–2471. [CrossRef]
4. Green, M.A.; Dunlop, E.D.; Hohl-Ebinger, J.; Yoshita, M.; Kopidakis, N.; Hao, X. Solar cell efficiency tables (version 59). *Prog. Photovolt. Res. Appl.* **2022**, *30*, 3–12. [CrossRef]
5. Stanbery, B.J. Copper Indium Selenides and Related Materials for Photovoltaic Devices. *Crit. Rev. Solid State Mater. Sci.* **2002**, *27*, 73–117. [CrossRef]
6. Islam, M.; Ishizuka, S.; Yamada, A.; Sakurai, K.; Niki, S.; Sakurai, T.; Akimoto, K. CIGS solar cell with MBE-grown ZnS buffer layer. *Sol. Energy Mater. Sol. Cells* **2009**, *93*, 970–972. [CrossRef]
7. Herman, F. Speculations on the Energy Band Structure of Ge—Si Alloys. *Phys. Rev.* **1954**, *95*, 847–848. [CrossRef]

8. Kemell, M.; Ritala, M.; Leskelä, M. Thin Film Deposition Methods for $CuInSe_2$ Solar Cells. *Crit. Rev. Solid State Mater. Sci.* **2005**, *30*, 1–31. [CrossRef]
9. Walsh, A.; Chen, S.; Gong, X.G.; Wei, S.H.; Ihm, J.; Cheong, H. Crystal structure and defect reactions in the kesterite solar cell absorber Cu_2ZnSnS_4 (CZTS): Theoretical insights. *AIP Conf. Proc.* **2011**, *1399*, 63–64. [CrossRef]
10. Liu, B.; Guo, J.; Hao, R.; Wang, L.; Gu, K.; Sun, S.; Aierken, A. Effect of Na doping on the performance and the band alignment of CZTS/CdS thin film solar cell. *Sol. Energy* **2020**, *201*, 219–226. [CrossRef]
11. Nugroho, H.S.; Refantero, G.; Septiani, N.L.W.; Iqbal, M.; Marno, S.; Abdullah, H.; Prima, E.C.; Nugraha; Yuliarto, B. A progress review on the modification of CZTS(e)-based thin-film solar cells. *J. Ind. Eng. Chem.* **2022**, *105*, 83–110. [CrossRef]
12. Nakazawa, K.I. Electrical and optical properties of stannite-type quaternary semiconductor thin films. *Jpn. J. Appl. Phys.* **1988**, *27*, 2094. [CrossRef]
13. Sun, K.; Liu, F.; Hao, X. Kesterite $Cu_2ZnSnS_{4-x}Se_x$ Thin Film Solar Cells. In *Thin Films Photovoltaics*; Zaidi, B., Shekhar, C., Eds.; IntechOpen: Rijeka, Croatia, 2021; Chapter 4. [CrossRef]
14. Yaseen, M.S.; Sun, J.; Fang, H.; Murtaza, G.; Sholl, D.S. First-principles study of electronic and optical properties of ternary compounds $AuBX_2$ (X = S, Se, Te) and $AuMTe_2$ (M = Al, In, Ga). *Solid State Sci.* **2021**, *111*, 106508. [CrossRef]
15. Moreau, A.; Insignares-Cuello, C.; Escoubas, L.; Simon, J.J.; Bermúdez, V.; Pérez-Rodríguez, A.; Izquierdo-Roca, V.; Ruiz, C.M. Impact of Cu–Au type domains in high current density $CuInS_2$ solar cells. *Sol. Energy Mater Sol. Cells* **2015**, *139*, 101–107. [CrossRef]
16. Kargar, A.; Hong, H.; Tower, J.; Gueorguiev, A.; Kim, H.; Cirignano, L.; Christian, J.F.; Squillante, M.R.; Shah, K. $LiInSe_2$ for Semiconductor Neutron Detectors. *Front. Phys.* **2020**, *8*, 78. [CrossRef]
17. Ma, C.G.; Brik, M. First principles studies of the structural, electronic and optical properties of $LiInSe_2$ and $LiInTe_2$ chalcopyrite crystals. *Solid State Commun.* **2015**, *203*, 69–74. [CrossRef]
18. Isaenko, L.; Yelisseyev, A.; Lobanov, S.; Krinitsin, P.; Petrov, V.; Zondy, J.J. Ternary chalcogenides $LiBC_2$ (B=In,Ga; C=S,Se,Te) for mid-IR nonlinear optics. *J. Non-Cryst. Solids* **2006**, *352*, 2439–2443. [CrossRef]
19. Petrov, V.; Isaenko, L.; Yelisseyev, A.; Krinitsin, P.; Vedenyapin, V.; Merkulov, A.; Zondy, J.J. Growth and characterization of the chalcopyrite $LiGaTe_2$: A highly non-linear birefringent optical crystal for the mid-infrared. *J. Non-Cryst. Solids* **2006**, *352*, 2434–2438. [CrossRef]
20. Tupitsyn, E.; Bhattacharya, P.; Rowe, E.; Matei, L.; Groza, M.; Wiggins, B.; Burger, A.; Stowe, A. Single crystal of $LiInSe_2$ semiconductor for neutron detector. *Appl. Phys. Lett.* **2012**, *101*, 202101. [CrossRef]
21. Lukosi, E.; Onken, D.; Hamm, D.; Brown, C.; Ievlev, A.V.; Burger, A.; Preston, J.; Williams, R.; Stowe, A. Intrinsic lithium indium diselenide: Scintillation properties and defect states. *J. Lumin.* **2019**, *205*, 346–350. [CrossRef]
22. Ranjan, P.; Chakraborty, T. A computational study of chalcopyrite-type nanomaterials for solar cell applications. *Mater. Sci. Semicond. Process* **2021**, *127*, 105745. [CrossRef]
23. Rudysh, M.Y.; Piasecki, M.; Myronchuk, G.L.; Shchepanskyi, P.A.; Stadnyk, V.Y.; Onufriv, O.R.; Brik, M.G. $AgGaTe_2$–The thermoelectric and solar cell material: Structure, electronic, optical, elastic and vibrational features. *Infrared Phys. Technol.* **2020**, *111*, 103476. [CrossRef]
24. Kushwaha, A.K.; Ma, C.G.; Brik, M.G.; Omran, S.B.; Khenata, R. Zone-center phonons and elastic properties of ternary chalcopyrite $ABSe_2$ (A = Cu and Ag; B = Al, Ga and In). *Mater. Chem. Phys.* **2019**, *227*, 324–331. [CrossRef]
25. Ma, C.G.; Liu, D.X.; Hu, T.P.; Wang, Y.; Tian, Y.; Brik, M.G. Ab initio calculations of the structural, electronic and elastic properties of the MZN_2 (M = Be, Mg; Z = C, Si) chalcopyrite semiconductors. *Sci. Adv. Mater.* **2016**, *8*, 466–475. [CrossRef]
26. Rudysh, M.Y.; Ftomyn, N.Y.; Shchepanskyi, P.A.; Myronchuk, G.L.; Popov, A.I.; Lemée, N.; Stadnyk, V.Y.; Brik, M.G.; Piasecki, M. Electronic Structure, Optical, and Elastic Properties of $AgGaS_2$ Crystal: Theoretical Study. *Adv. Theory Simul.* **2022**, *5*, 2200247. [CrossRef]
27. Chen, S.; Gong, X.G.; Wei, S.H. Band-structure anomalies of the chalcopyrite semiconductors $CuGaX_2$ versus $AgGaX_2$ (X = S and Se) and their alloys. *Phys. Rev. B* **2007**, *75*, 205209. [CrossRef]
28. Jiang, X.; Lambrecht, W.R.L. Electronic band structure of ordered vacancy defect chalcopyrite compounds with formula $II - III_2 - VI_4$. *Phys. Rev. B* **2004**, *69*, 035201. [CrossRef]
29. Rudysh, M.; Shchepanskyi, P.; Fedorchuk, A.; Brik, M.; Stadnyk, V.; Myronchuk, G.; Kotomin, E.; Piasecki, M. Impact of anionic system modification on the desired properties for CuGa $(S-Se)^2$ solid solutions. *Comput. Mater. Sci.* **2021**, *196*, 110553. [CrossRef]
30. Beister, H.J.; Ves, S.; Hönle, W.; Syassen, K.; Kühn, G. Structural phase transitions and optical absorption of $LiInSe_2$ under pressure. *Phys. Rev. B* **1991**, *43*, 9635–9642. [CrossRef]
31. Sangalli, D.; Ferretti, A.; Miranda, H.; Attaccalite, C.; Marri, I.; Cannuccia, E.; Melo, P.; Marsili, M.; Paleari, F.; Marrazzo, A.; et al. Many-body perturbation theory calculations using the yambo code. *J. Phys. Condens. Matter* **2019**, *31*, 325902. [CrossRef]
32. Ullrich, C. *Time-dEpendent Density-Functional Theory: Concepts and Applications*; Oxford Graduate Texts; Oxford University Press: Oxford, UK; New York, NY, USA, 2012.
33. Dovesi, R.; Saunders, V.R.; Roetti, C.; Orlando, R.; Zicovich-Wilson, C.M.; Pascale, F.; Civalleri, B.; Doll, K.; Harrison, N.M.; Bush, I.J.; et al. *CRYSTAL17 User's Manual*; University of Torino: Torino, Italy, 2017.
34. Dovesi, R.; Erba, A.; Orlando, R.; Zicovich-Wilson, C.M.; Civalleri, B.; Maschio, L.; Rérat, M.; Casassa, S.; Baima, J.; Salustro, S.; et al. Quantum-mechanical condensed matter simulations with CRYSTAL. *Wiley Interdiscip. Rev. Comput. Mol. Sci.* **2018**, *8*, e1360. [CrossRef]

35. Evarestov, R.A.; Bandura, A.V.; Losev, M.V.; Kotomin, E.A.; Zhukovskii, Y.F.; Bocharov, D. A first-principles DFT study of UN bulk and (001) surface: Comparative LCAO and PW calculations. *J. Comput. Chem.* **2008**, *29*, 2079–2087. [CrossRef] [PubMed]
36. Giannozzi, P.; Andreussi, O.; Brumme, T.; Bunau, O.; Nardelli, M.B.; Calandra, M.; Car, R.; Cavazzoni, C.; Ceresoli, D.; Cococcioni, M.; et al. Advanced capabilities for materials modelling with Quantum ESPRESSO. *J. Phys. Condens. Matter* **2017**, *29*, 465901. [CrossRef] [PubMed]
37. Marini, A.; Hogan, C.; Grüning, M.; Varsano, D. Yambo: An ab initio tool for excited state calculations. *Comput. Phys. Commun.* **2009**, *180*, 1392–1403. [CrossRef]
38. Peintinger, M.F.; Oliveira, D.V.; Bredow, T. Consistent Gaussian basis sets of triple-zeta valence with polarization quality for solid-state calculations. *J. Comput. Chem.* **2013**, *34*, 451–459. [CrossRef]
39. Heyd, J.; Scuseria, G.E.; Ernzerhof, M. Hybrid functionals based on a screened Coulomb potential. *J. Chem. Phys.* **2003**, *118*, 8207–8215. [CrossRef]
40. BROYDEN, C.G. The Convergence of a Class of Double-rank Minimization Algorithms: 2. The New Algorithm. *IMA J. Appl. Math.* **1970**, *6*, 222–231. [CrossRef]
41. Perdew, J.; Wang, Y. Accurate and simple analytic representation of the electron-gas correlation energy. *Phys. Rev. B.* **1986**, *33*, 8800. [CrossRef]
42. Perdew, J.; Wang, Y. Pair-distribution function and its coupling-constant average for the spin-polarized electron gas. *Phys. Rev. B.* **1989**, *40*, 3399. [CrossRef]
43. Perdew, J.; Wang, Y. Accurate and simple density functional for the electronic exchange energy: Generalized gradient approximation. *Phys. Rev. B.* **1992**, *45*, 13244. [CrossRef]
44. Becke, A. Density-functional thermochemistry. III. The role of exact exchange. *J. Chem. Phys.* **1993**, *98*, 5648. [CrossRef]
45. Becke, A. Density-functional exchange-energy approximation with correct asymptotic behavior. *Phys. Rev. B.* **1988**, *38*, 3098. [CrossRef] [PubMed]
46. Lee, C.; Yang, W.; Parr, R. Development of the Colle-Salvetti correlation-energy formula into a functional of the electron density. *Phys. Rev. B.* **1988**, *37*, 785. [CrossRef] [PubMed]
47. Janesko, B.G.; Henderson, T.M.; Scuseria, G.E. Screened hybrid density functionals for solid-state chemistry and physics. *Phys. Chem. Chem. Phys.* **2009**, *11*, 443–454. [CrossRef]
48. Ernzerhof, M.; Scuseria, G.E. Assessment of the Perdew–Burke–Ernzerhof exchange-correlation functional. *J. Chem. Phys.* **1999**, *110*, 5029–5036. [CrossRef]
49. Schmider, H.L.; Becke, A.D. Exchange holes that accurately reproduce the first-order density matrix and the nature of the corresponding exchange potentials. *J. Chem. Phys.* **1998**, *108*, 962–969. [CrossRef]
50. Tinoco, T.; Rincón, C.; Quintero, M.; Pérez, G.S. Phase Diagram and Optical Energy Gaps for $CuIn_yGa_{1-y}Se_2$ Alloys. *Phys. Status Solidi (a)* **1991**, *124*, 427–434. [CrossRef]
51. Setten, M.J.v.; Giantomassi, M.; Bousquet, E.; Verstraete, M.J.; Hamann, D.R.; Gonze, X.; Rignanese, G.M. The PseudoDojo: Training and grading a 85 element optimized norm-conserving pseudopotential table. *Comput. Phys. Commun.* **2018**, *226*, 39–54. [CrossRef]
52. Perdew, J.P.; Burke, K.; Ernzerhof, M. Generalized Gradient Approximation Made Simple. *Phys. Rev. Lett.* **1996**, *77*, 3865–3868. [CrossRef]
53. Aroyo, M.I.; Perez-Mato, J.M.; Orobengoa, D.; Tasci, E.; de la Flor, G.; Kirov, A. Crystallography online: Bilbao crystallographic server. *Bulg. Chem. Commun* **2011**, *43*, 183–197.
54. Rife, J.C.; Dexter, R.N.; Bridenbaugh, P.M.; Veal, B.W. Optical properties of the chalcopyrite semiconductors $ZnGeP_2$, $ZnGeAs_2$, $CuGaS_2$, $CuAlS_2$, $CuInSe_2$, and $AgInSe_2$. *Phys. Rev. B* **1977**, *16*, 4491–4500. [CrossRef]
55. Ahuja, R.; Auluck, S.; Eriksson, O.; Wills, J.M.; Johansson, B. Calculated optical properties of a solar energy material: $CuGaS_2$. *Sol. Energy Mater. Sol. Cells* **1998**, *53*, 357–366. [CrossRef]
56. Levcenko, S.; Syrbu, N.N.; Tezlevan, V.E.; Arushanov, E.; Doka-Yamigno, S.; Schedel-Niedrig, T.; Lux-Steiner, M.C. Optical spectra and energy band structure of single crystalline $CuGaS_2$ and $CuInS_2$. *J. Condens. Matter Phys.* **2007**, *19*, 456222. [CrossRef]
57. Regolini, J.L.; Lewonczuk, S.; Ringeissen, J.; Nikitine, S.; Schwab, C. Optical Properties of $CuGaS_2$ near the Fundamental Absorption Edge. *Phys. Status Solidi B* **1973**, *55*, 193–200. [CrossRef]
58. Blase, X.; Duchemin, I.; Jacquemin, D.; Loos, P.F. The Bethe–Salpeter Equation Formalism: From Physics to Chemistry. *J. Phys. Chem. Lett.* **2020**, *11*, 7371–7382. [CrossRef]
59. Gao, W.; Xia, W.; Gao, X.; Zhang, P. Speeding up GW Calculations to Meet the Challenge of Large Scale Quasiparticle Predictions. *Sci. Rep.* **2016**, *6*, 36849. [CrossRef] [PubMed]